

# Analysis of the 3D microstructure of tape-cast open-porous materials via a combination of experiments and modeling

S. Haj Ibrahim <sup>\*a</sup>, M. Neumann <sup>b</sup>, F. Klingner <sup>b</sup>, V. Schmidt <sup>b</sup>, T. Wejrzanowski <sup>a</sup>

<sup>a</sup> Warsaw University of Technology, Faculty of Materials Science and Engineering  
Woloska 141, 02507 Warsaw, Poland

<sup>b</sup> Ulm University, Institute of Stochastics, Helmholtzstraße 18, 89069 Ulm, Germany

\* Corresponding author's e-mail address: samihhaj.ibrahim@inmat.pw.edu.pl

E-mails: matthias.neumann@uni-ulm.de (M. Neumann), frederik.klingner@uni-ulm.de (F. Klingner),  
volker.schmidt@uni-ulm.de (V. Schmidt), twejrzanowski@inmat.pw.edu.pl (T. Wejrzanowski)

## Abstract

In the present paper, fabrication, characterization and modeling techniques are combined to analyze the microstructure of tape-cast open-porous materials. This kind of material is highly permeable to gases and at the same time has a high catalytic reactivity which leads to successful applications e.g. in high-temperature fuel cells. However, the microstructure of such material is complex and not fully understood. The main goal of this paper is to provide a realistic model of tape-cast porous microstructures based on the simulation of their fabrication process. In order to accomplish this, four different samples are fabricated by firing the green tapes obtained by the tape casting process. The microstructure of each sample is analyzed by means of micro-tomographic image data. Furthermore, a method for modeling open-porous 3D microstructures is proposed, where the cast slurry is represented by a system of spheres with a given volume fraction and radius distribution. Model-based post-processing of the simulated microstructures is proposed to improve the fit of the surface area. Finally, model validation is performed by means of a detailed statistical analysis of experimentally produced and virtual microstructures.

**Keywords:** Open-porous materials, 3D microstructure modeling, micro-computed tomography, molten carbonate fuel cell

## 1. Introduction

Apart from chemical and phase composition, the 3D microstructure has a strong influence on the macroscopic properties of many functional materials [1]. For open-porous materials used in fuel cells, porosity, pore size distribution and specific surface area are crucial parameters for the efficiency of the cell [2,3]. The 3D microstructure is even more important in molten carbonate fuel cells (MCFC), where a specific pore size distribution is required for the electrodes to be properly penetrated by the liquid carbonate electrolyte. Since the cathode is typically made of porous nickel, it oxidizes in situ, which causes a reduction of porosity and pore size [4,5]. The processes taking place at the cathode side are the slowest ones over the entire cell kinetics [6,7]. Thus, the optimization of cathode microstructures seems to be the most challenging issue for the improvement of cell efficiency. One should note that the efficiency and durability of the cell depends on three main phenomena [8], which are 1) the gas transport to the triple-phase reaction zone (electrode, electrolyte, gas), where the electrolytic reaction occurs, 2) the decomposition of gas molecules at that area, and 3) the diffusion of ions through the electrolyte. The kinetics of each process depends on the competing properties of the porous 3D microstructure. Gas transport is more efficient for higher porosity and larger pores, while structures with fine pores and large specific surface area are better for catalysis. Due to the complexity of these processes a systematic optimization of the material is needed rather than a trial-and-error approach.

Mathematical modeling of the fabrication processes and microstructures of open-porous materials may lead to the efficient design of novel materials with improved properties.

Materials for electrodes (both, cathodes and anodes) of MCFC are typically fabricated using a tape casting technique by the firing of green tapes, which forms porous microstructures after annealing [9]. This method allows one to control the characteristics of the 3D microstructure of the electrode by adjusting the slurry composition along with the casting and firing conditions [10]. Furthermore, this fabrication technique leads to an open-porous microstructure and, although the technique is relatively simple, the resulting 3D microstructure is complex. One direct approach to investigate the influence of such open-porous microstructures on macroscopic properties, like the efficiency of the cell, is based on the usage of tomographic image data, see e.g. [11,12]. Using tomographic image data, well-defined structural characteristics can be computed and their influence on macroscopic properties, either measured by physical experiments or simulated by numerical modeling, can be investigated. For an overview of numerical models for MCFC, we refer to the introductory part of [13] and the references therein.

However, due to the high costs of tomographic imaging, one is limited in the number of 3D images that can be obtained in this way. Thus, it is not possible to investigate structural scenarios for a large variety of production parameters, which must be optimized with respect to cell efficiency and durability. Alternatively, predictive computer simulations based on mathematical modeling can be used to generate a wide spectrum of virtual, but realistic microstructures. A selection of elementary model types is given in [14] and examples can be found in [11,15,16] for modeling open-porous structures in cellular materials, and in [12] for modeling the microstructure of cathodes used in solid oxide fuel cells (SOFC). The virtual microstructures can be used as an input for numerical modelling to compute the corresponding macroscopic properties. In this way, a wide spectrum of porous microstructures can be systematically investigated with the general goal of determining the preferred microstructures, which exhibit improved macroscopic properties [17,18]. A review of the state-of-the-art of numerical modeling of macroscopic properties of microstructures on different length scales is given in [19].

With respect to MCFC, the numerical simulation of their macroscopic properties is mostly based on an agglomerate model for the porous microstructures in the electrodes [20]. The existence of two kinds of pores is the main assumption in this model: the micro-pores inside agglomerates, which are completely flooded with the electrolyte, and larger cylindrical macro-pores between agglomerates, which contain only gas. However, geometrical restrictions in the agglomerate model create difficulties in modeling electrolyte-filling [21] as well as in determining an optimal pore radius and an optimal film thickness [22]. Other approaches, like granular or meta-ball models, have been developed to deal with these issues, which make it possible to achieve representative models with a higher conformity of structural parameters to those of the real materials [12,23]. However, these methodologies are not based on the formation process so it is not possible to directly create new structural scenarios for different manufacturing parameters, and therefore they still need imaged structures as an input. In the present paper, we propose a more comprehensive model of the microstructure, which can simulate the fabrication process of the MCFC cathodes itself and not only its output. The model also allows one to control the volume fraction and further features of substrates used in experiments and enables one to model a wide spectrum of new structures, even those not manufactured before. Such an approach facilitates the design of new materials with improved properties, which can then be fabricated and used for the electrodes of MCFC.

The rest of the paper is organized as follows. In Section 2, we describe the fabrication process and the tomographic imaging of experimental microstructures, while in Section 3 we present the microstructure model for simulation of the fabrication process and methods for the quantitative characterization of both, image data of experimental microstructures as well as image data of virtual microstructures generated by the model. This quantitative characterization leads to a validation of the model, which is discussed in Section 4. Section 5 concludes the paper.

## 2. Experimental methods

### 2.1. Fabrication procedure

Four different MCFC cathode samples have been fabricated by a two-step process, which involves tape casting and firing procedures. A schematic illustration of the technical set-up is shown in Figure 1.

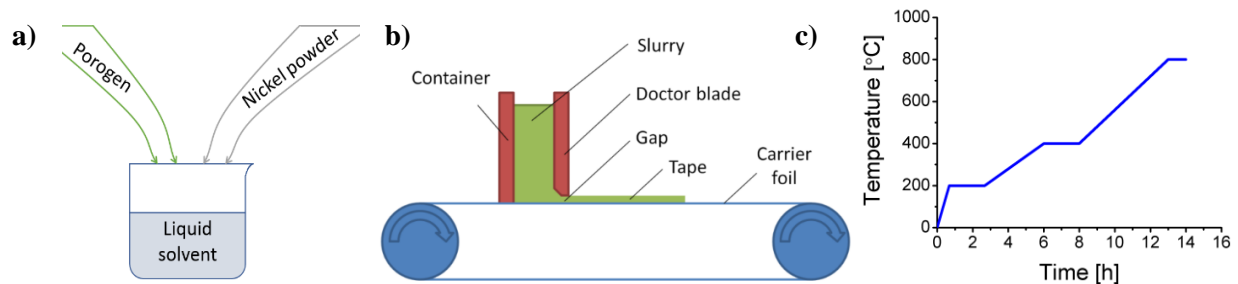


Fig. 1. Schematic illustration of the slurry composition (a), set up of the tape casting process (b), and temperature program of the firing process (c).

The slurry for the casting of the green tapes is obtained by the mechanical mixing of nickel powder with water, polymeric binder (Carboxymethyl cellulose – CMC), porogen (starch) and other additives (i.e. dispersant, defoamer). The size distributions of nickel and porogen particles (see Figure 2) have been measured by the laser diffraction method [24] (Kamika IPS U). The compositions of the slurries differ in the fraction of porogen (see Table 1). Each slurry is cast on a glass surface with velocity 0.5 mm/s, through the gap in a doctor blade of height 1 mm.

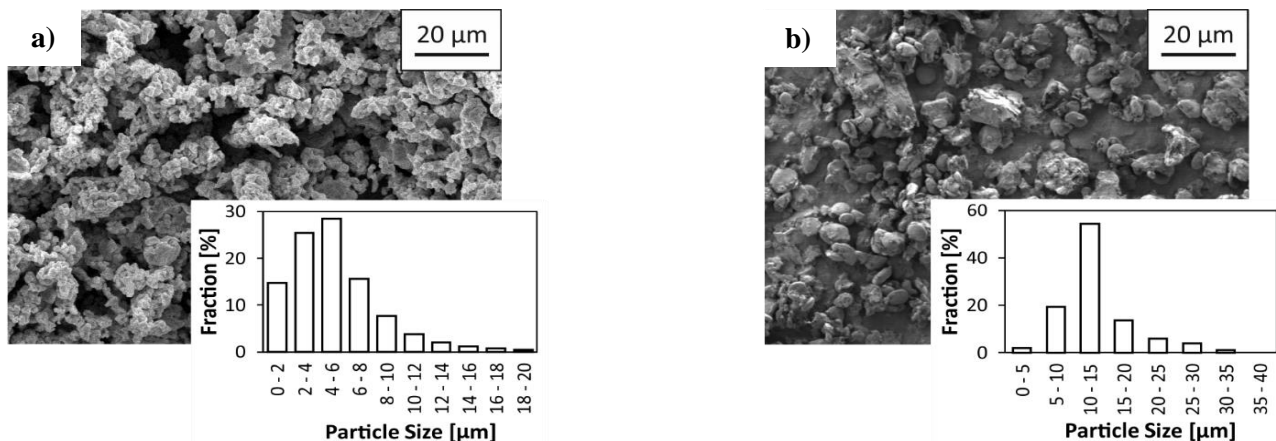


Fig. 2. Particle size distribution and SEM images of nickel (a) and starch (b).

After drying for one day at room temperature, flexible green tapes (see Figure 3a) are fired at a controlled temperature program (see Figure 1c) and at reducing atmosphere ( $N_2+5\%H_2$ ). Heat treatment can be separated into three steps: removing of volatile components (low temperature step), firing of binder residues (middle temperature step), sintering of Ni powder (high temperature step). An appropriate thermal regime is especially important, since it affects the porosity of the material [25]. As a result, an open-porous structure of the sintered tape is obtained (see Figure 3b,c).

Table. 1. Composition of the slurries used for casting of green tapes.

Sample	Nickel powder	Liquid phase	Porogen
	wt%	wt%	wt%
1	55.0	42.5	2,5
2	55.0	40.0	5,0
3	55.0	37.5	7,5
4	55.0	35.0	10,0

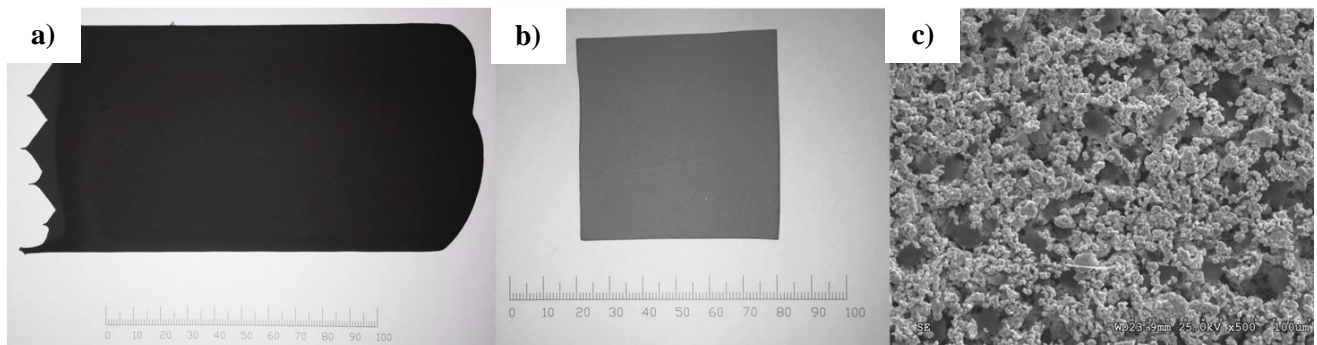


Fig. 3. Green tape (a), sintered tape (b), and SEM image of the obtained open-porous MCFC cathode (c).

## 2.2. Tomographic reconstruction of 3D microstructure

The manufactured cathode materials are characterized by micro-computed tomography ( $\mu$ CT), which is conducted using a high-resolution Xradia XCT-400 instrument under an acceleration of 40kV, and a current of 10 A with a resolution of  $0.6\mu\text{m}$  per voxel. For each sample, a region of about  $400\mu\text{m} \times 400\mu\text{m} \times 400\mu\text{m}$  is imaged. The 3D images are reconstructed from 2D radiography images with XCT-reconstruction software (see Figure 4). In this way, 3D structures are obtained, where each 3D image is given as a stack of nearly one thousand 2D greyscale images (in an 8bit-format). The Otsu algorithm [26] is used to binarize the images by automatic thresholding. Small speckles in the images are removed to reduce the noise.

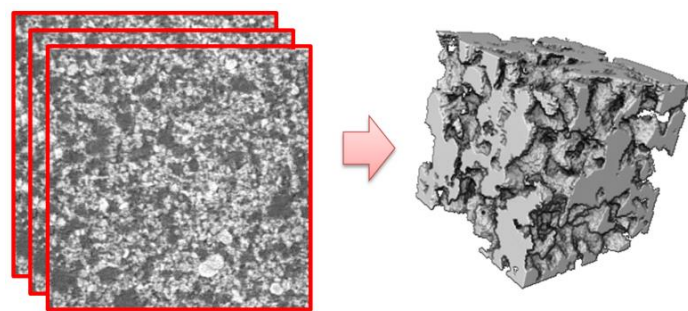


Fig. 4. Reconstruction of 3D material structure from a sequence of 2D images.

### 3. Modeling and simulation

#### 3.1. Model driven by the fabrication process

A mathematical model for the 3D microstructure of open-porous materials is obtained using a multistep algorithm implemented in the software LAMMPS [27,28], which is a molecular dynamics simulator which includes the generation and packing of spheres. In order to model the fabrication process, a slurry model is used with three types of spheres representing nickel powder particles, liquid phase, and porogen. The particle size distributions of substrate powder and the volume fractions of the real slurry components are utilized as input parameters to create an initial sphere system, while the radii of the spheres representing the liquid phase are constant at  $1\mu\text{m}$ , which is the minimum value due to computational limitations. In this way, 100 000 non-overlapping spheres are generated in 3D space with random positions and radii (see Figure 5a). The packing process is divided into two steps: 1) densification of the initial (sparse) sphere system to create the slurry model and 2) simulation of the sintering process. In the first step of the packing process, Hertzian pairwise interaction is utilized [27] and spheres are packed with npt/sphere fixing (Nose/Hoover ensemble) [28] with a slight compression (pressure 0.1 MPa). This results in a shrinkage of the simulation box and in a denser packing of the spheres. The densification is stopped when the increase of volume fraction is lower than 0.01%. Using this procedure, a slurry model is created (see Figure 5b). The modeling of the sintering process requires an additional pairwise potential between powder particles to join them together. The Lennard-Jones potential, see e.g. [29], is used for this purpose. More details regarding the Hertzian pairwise interaction and the Lennard-Jones potential can be found in Appendix A. During the simulation of the sintering process, spheres representing liquid phase and porogen are gradually removed. Furthermore, a gravity field is applied and, consequently, no hanging particles are present afterwards. As a result, a model of the 3D microstructure after the sintering process is obtained (see Figure 5c). Additional smoothing is applied to create a single entity from the set of spheres and to obtain realistic narrow connections between the spheres after Gaussian smoothing [30], similar to the necks observed in real sintered materials (see Figure 5d).

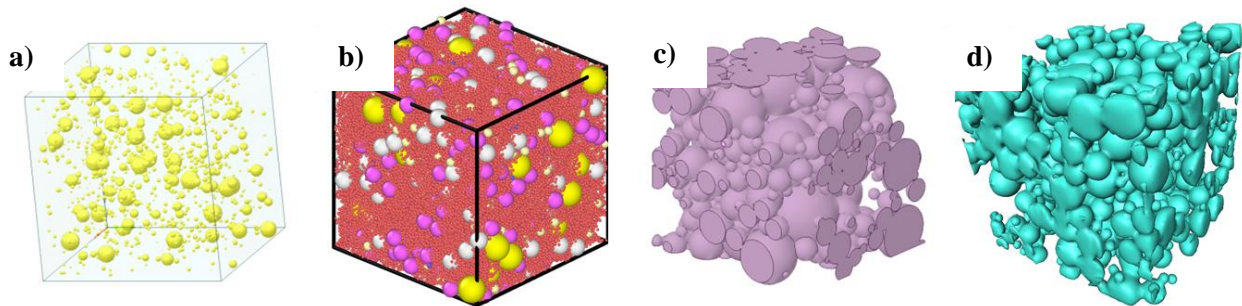


Fig. 5. Initial sphere system (a), packed slurry model (b), microstructure after modeling of the sintering process (c), and after Gaussian smoothing (d).

For each porogen concentration, we generate 10 realizations of virtual microstructure using our modeling procedure to provide a sufficiently large data basis for our statistical analysis. Thus, in total, 40 virtual microstructures are created. The box size of each virtual microstructure is about  $100\mu\text{m} \times 100\mu\text{m} \times 100\mu\text{m}$  and periodic boundary conditions are applied.

The analysis of the model realizations, produced in this way, shows that the values of the specific surface area of the solid phase follow a trend of being smaller in the model than the values estimated from experimental image data. The reason for this is that the solid powder particles are represented by ideal spheres. Thus, we apply a slightly modified version of the algorithm presented in [12], which increases the surface area of a binary 3D microstructure with almost no changes in its volume fraction. The surface area is increased by adding and removing small spheres with radius  $r_0 > 0$  at the surface of the set union of the original sphere system (see Figure 6). The midpoints of these small spheres are modeled by two (successively considered)

Matérn hard-core point processes [14] with a hard-core radius of  $r_0$  on the surface of the original sphere system. Thereby, a further condition for the second process is that all generated points must have the same minimum distance  $r_0$  to all previously generated points. In a single Matérn hard-core point process, the points are (conditionally) distributed completely at random on the surface with a certain intensity  $\lambda > 0$ , under the condition that there is a minimum distance of  $r_0$  between each pair of (mid-) points. Having simulated the midpoints of small spheres on the surface of the original sphere system, each small (half) sphere is either added to or removed from the solid phase with probability  $1/2$ . After this random surface roughening, all major parts of the original sphere system should still be connected to each other. Thus, we impose a further rule, which states that a small sphere is not added or removed from the solid phase if it overlaps with the centerlines of the original sphere system, see Figure 6a. The centerlines are computed by the skeletonization algorithm presented in [31].

For a fixed hard-core radius  $r_0 = 3.6\mu\text{m}$ , the parameter  $\lambda$  is fitted in order to minimize the differences in the surface areas between model and image data regarding all four material scenarios. To accomplish this, we use the bisection method. After the surface roughening described above, we remove all clusters of the solid phase (always excluding the largest one) which are not connected to at least one boundary of the corresponding images. A 2D slice of a model realization after surface roughening and subsequent removal of non-connected clusters is visualized in Figure 6b.

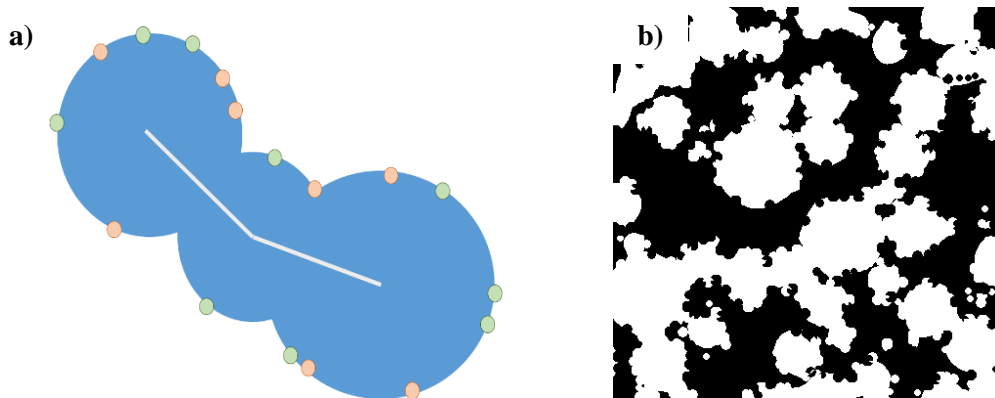


Fig. 6. Schematic representation of the modeling idea for the surface-roughening algorithm (a), where the centerlines of the solid phase are drawn in white, and a 2D slice of a model realization after surface roughening and subsequent removal of non-connected clusters (b).

### 3.2. Methods for quantitative characterization of experimental and virtual microstructures

To fit and validate the model, quantitative image analysis is performed on image data of both, experimental microstructures and virtual microstructures generated by the model. The output of a model realization consists of vector data, describing the sphere system. This vector data is discretized on a voxel grid with the same resolution as the voxel grid of the  $\mu\text{CT}$  images representing experimental microstructures, i.e., with a resolution of  $0.6\mu\text{m}$ . By doing so, we obtain a set of 3D images, given as stacks of 2D images. To process the 3D image data, we use the software Avizo [32].

The first stage of our quantitative analysis is to choose a representative volume element (RVE) with respect to local spatial heterogeneity. In order to accomplish that, the (local) porosity of 45 randomly placed, cubic sub-regions (regions of interest – ROI) with increasing size was calculated. Furthermore, we analyze the correlation function of the solid phase, which is called the pair-correlation function [14]. Note that the correlation function of the solid phase can be used to describe the range of dependence within the microstructure. If the value of the correlation function evaluated for some image data at position  $r$  is equal to 1, then no correlation exists between voxels with distance  $r$  to each other. For all four samples, the correlation function is calculated for

cubic subregions cut out from the three-dimensional  $\mu$ CT images, the size of which is the same as the one of the model realizations. The SkyScan CT analyzer and software Avizo are used to characterize the global and local microstructure parameters, such as porosity and mean pore size [33]. For the computation of the surface area, we use the method presented in [34]. The mean geodesic tortuosity, which is a measure of the windedness of transport paths [35], is computed by means of the software library GeoStoch [36].

The quantitative characterization of virtual microstructures is performed on 10 model realizations for each amount of porogen given in Table 1. This corresponds to the procedure used for the experimental microstructures, where 45 randomly selected subregions (with the same size as the virtual microstructures, i.e.,  $100\mu\text{m} \times 100\mu\text{m} \times 100\mu\text{m}$ ) are used for the characterization of each sample.

#### 4. Results and discussion

To determine the smallest possible RVE, we compute the porosity for a sequence of growing ROI (see Figure 7). The results show that, independently of the considered amount of porogen, the standard deviation of porosity decreases and stabilizes at 1-2% for ROI sizes of about  $200\mu\text{m}$ . For a ROI size of  $100\mu\text{m}$  (which is the size that the model produces) the standard deviation of porosity is 4-5%.

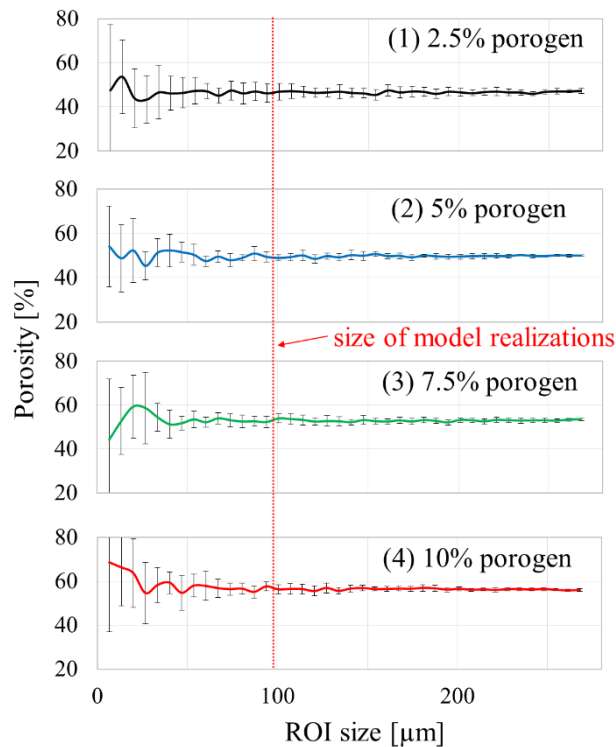


Fig. 7. Evolution of porosity with growing ROI for the three-dimensional  $\mu$ CT images. Error bars indicate  $\pm$  standard deviation of the porosity.

For all four amounts of porogen considered in the present paper, the values of the correlation functions are close to 1 for distances larger than  $25\mu\text{m}$  (see Figure 8). This suggests that the size used for the model realizations considered in the present paper ( $100\mu\text{m}$  side cube) is big enough with respect to their range of dependence.

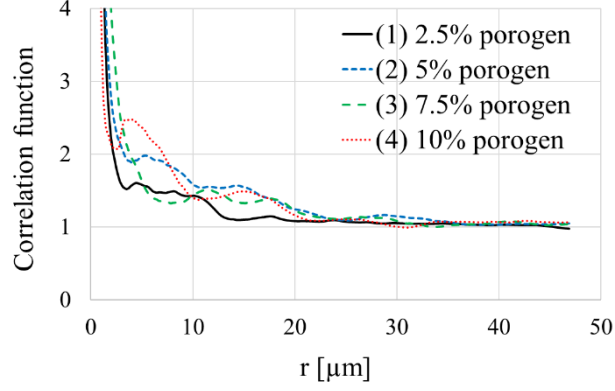


Fig. 8. Correlation function for the three-dimensional  $\mu$ CT images.

In Figure 9, the values of porosity and mean pore size estimated from experimental  $\mu$ CT images and model realizations are shown. Both, porosity and mean pore size increase with an increasing amount of porogen. This trend is faithfully reproduced by our virtual microstructural model. The standard deviation of porosity, marked as error bars, is larger in the experimental image data than in the simulated data, which indicates a higher local heterogeneity for real microstructures. This might be related to the powder aggregation process, which is not present in the model.

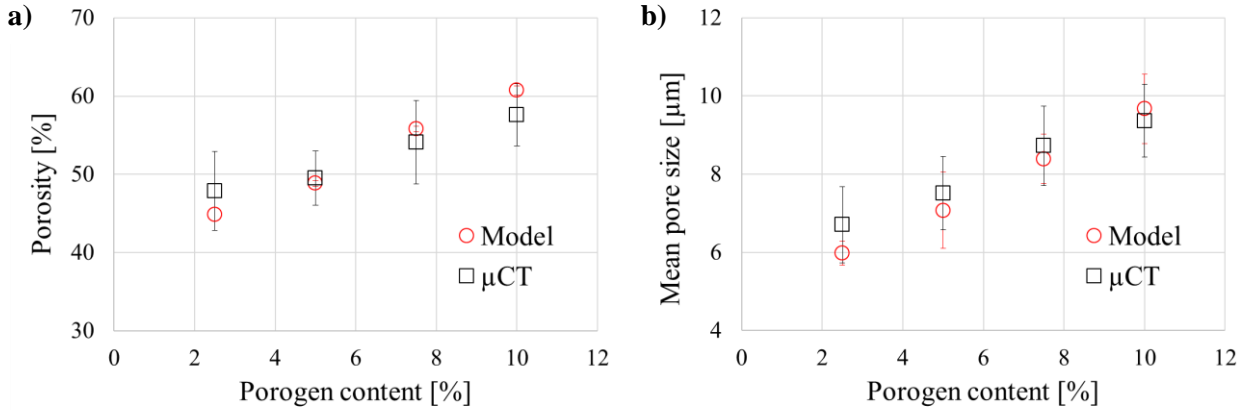


Fig. 9. The influence of initial porogen content on porosity of final microstructures (a) and their mean pore size (b). Error bars indicate  $\pm$  standard deviation.

Although our modeling procedure reproduces the trend of porosity quite well with respect to an increasing amount of porogen, Figure 9 also shows that the porosities of the model do not perfectly fit the porosities of tomographic image data. But there is no general trend of over- or underestimation of porosity that can be observed. However, in the following, we present a method of how to further improve the fit of the porosity for a given amount of porogen, which is based on a small modification of the roughening algorithm presented in Section 2.3.

So far, small spheres, the midpoints of which are randomly located at the surface of the material, are added with probability  $p = 1/2$  and removed with probability  $1 - p = 1/2$ . If we consider the probability  $p$  as a model parameter between 0 and 1, which is estimated for each porogen scenario separately, it is possible to adjust the volume fraction of the model realizations more precisely. Assume that by adding a sphere, the midpoint of which is located on the surface of the material, it adds half of its volume to the material. An analogous assumption is made for removing spheres. Then, given that the number of all points of the point pattern at the surface equals  $N$ , the increase of porosity, denoted by  $\Delta P$  can be approximated by

$$\Delta P \approx ((1 - p) - p) \frac{N}{V} \frac{2}{3} \pi r^3, \quad (3)$$

where  $V$  denotes the volume of the observation window. This leads to the following estimator  $\hat{p}$  for  $p$ :

$$\hat{p} = \min \left\{ \max \left\{ \frac{1}{2} \left( \frac{3V\Delta P}{2N\pi r^3} + 1 \right), 0 \right\}, 1 \right\}, \quad (4)$$

Using the value of  $\hat{p}$  for the model parameter  $p$ , we are able to generate virtual microstructures, where the porosity can be further adjusted, see Figure 10. Note that the difference in surface area is neglectable when changing the value of  $p$ , i.e. changing the ratio of added and removed spheres.

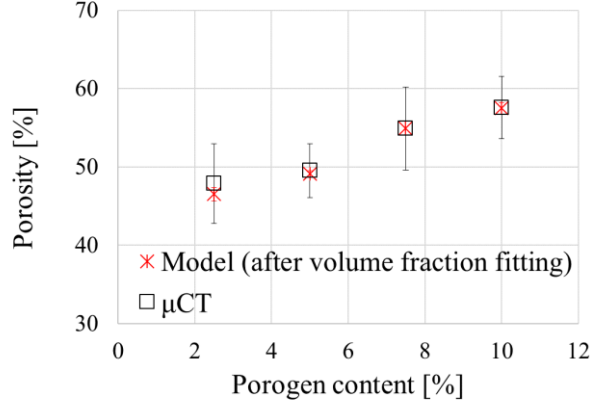


Fig. 10. Porosity results after individual volume fraction fitting for each porogen scenario.

However, with this refinement of the microstructure model, we would have to introduce a further parameter which depends on the considered material (i.e. the content of porogen) and which is not directly related to the fabrication process. Thus, it depends on the given application of the model if the refined model should be considered or not. In other words, one has to decide whether a perfect match of porosity is more important than having a model which depends exclusively on the fabrication process. In the rest of the present paper, we discuss the properties of the model without this additional refinement, because one of the major advantages of our model is its ability to predict microstructures for any given amount of porogen, including those for which no  $\mu$ CT-images are available. Of course, in this case, it is not possible to estimate the parameter  $p$ .

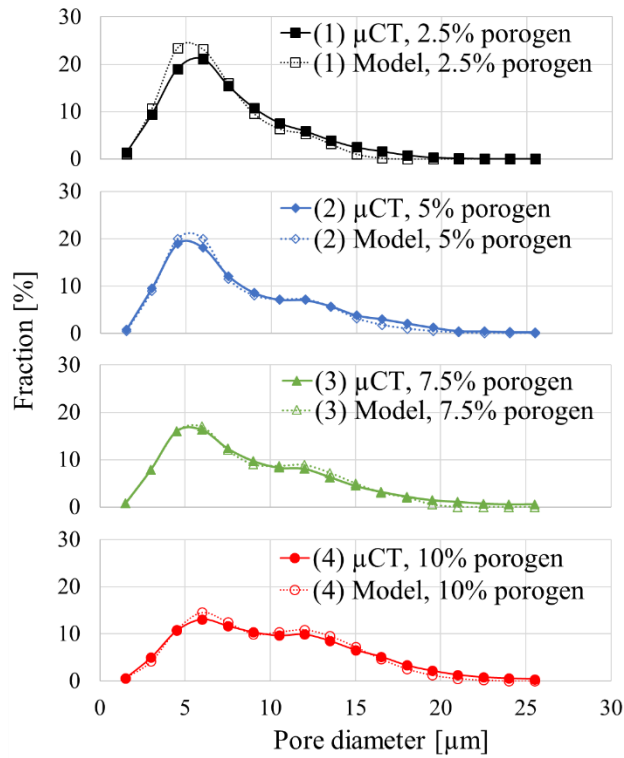


Fig. 11. Pore size distribution for three-dimensional  $\mu$ CT images and model realizations.

Besides porosity, the pore size distribution is computed for experimental image data and for model realizations. The results are displayed in Figure 11. Note that the modeling procedure developed in the present paper reproduces the distribution of pore sizes observed in experimental image data accurately, although the fraction of larger pores is slightly higher in experimental image data than in the virtual microstructures generated by the model.

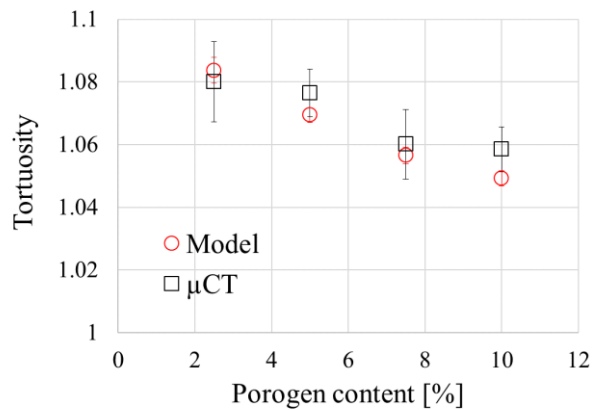


Fig. 12. The influence of initial porogen content on mean geodesic tortuosity.

The results obtained for mean geodesic tortuosity are shown in Figure 12. It can be observed that increasing porogen content results in a lower tortuosity of the manufactured structures. The explanation for this relationship might be the greater pore volume, which decreases the number of obstacles, encountered by a flowing reagent, and thus, shortens the flow distance. Similar to the other microstructure characteristics, the values of mean geodesic tortuosity estimated from model realizations are consistent with those values estimated from experimental image data, where the standard deviation of mean geodesic tortuosity is slightly

lower in the virtual microstructures generated by our modeling procedure. Since mean geodesic tortuosity is a transport-relevant microstructural characteristic [35], a good fit is important for further investigations, in which microstructural modeling will be combined with the numerical simulation of flow.

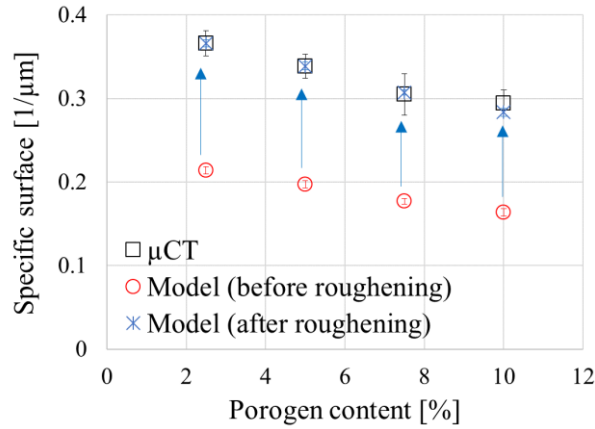


Fig. 13. Specific surface area before and after surface roughening.

The results, which we obtained for the specific surface area, are shown in Figure 13. It turns out that an increasing amount of porogen results in smaller values of the specific surface area. This is consistent with our findings for the mean pore size – larger pore sizes cause a decrease in the specific surface area. However, a large discrepancy between experimental image data and model realizations is observed if no surface roughening is considered, see Figure 13. This is caused by the fact that the powder particles in the model are then heavily idealized, by representing them by spheres, which are characterized by the smallest ratio of surface area to volume. Real powder particles exhibit a much higher surface area, which results in the higher specific surface area of the obtained structure. To reflect the shape effect of powder particles, we apply the surface roughening described in Section 2 to model realizations (see also Figure 14).

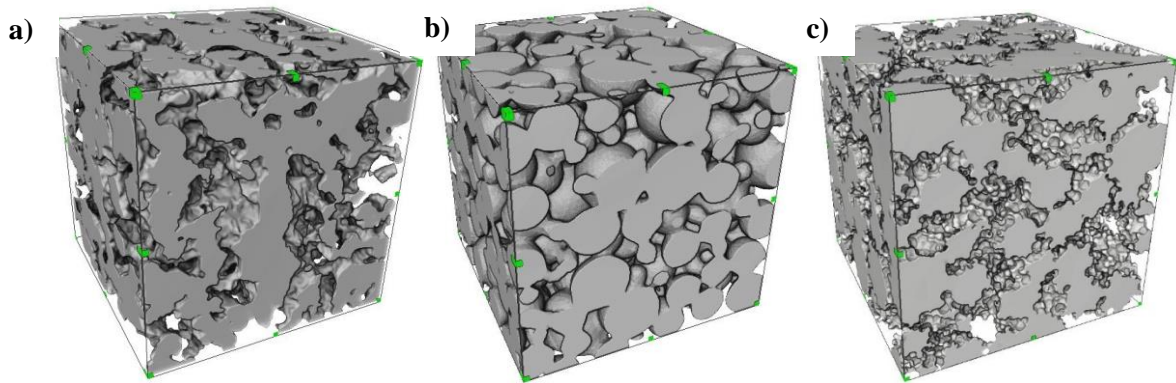


Fig. 14. Tomographic image data after binarization (a), realization of the initial microstructure model before (b) and after surface roughening (c).

Our numerical results indicate that the surface roughening of the simulated sphere systems leads to an appropriate increase in the specific surface area (see Figure 13) and, consequently, to a microstructural model with improved morphological properties, being much closer to those of real structures. A certain drawback of the model is its relatively small heterogeneity, which is smaller than in real materials. This will be the direction of our future research for further improvements of the model proposed in the present paper.

## 5. Conclusions

In the present paper, a modeling approach for open-porous materials including their fabrication process was established. The main conclusions and findings can be listed as follows:

- A comprehensive analysis of the 3D microstructure of MCFC cathodes was performed.
- Novel methodology for modeling the open-porous structures of the 3D microstructures of MCFC cathodes based on their manufacturing process was presented.
- It was shown that this methodology can be applied to model realistic virtual microstructures with microstructure characteristics similar to those of real materials.
- The advantages and disadvantages of the presented approach were discussed. A modification of the model for further improvement of the fit of specific surface area was proposed.
- Using these results, it was possible to investigate the relationships between the descriptors of the fabrication process and structural characteristics.

In a forthcoming paper, the developed microstructural model will be used to study various further processes taking place in open-porous materials and, in particular, in Molten Carbonate Fuel Cells (MCFC), which includes such processes as the infiltration of electrodes by the liquid electrolyte and the reactive flow of gases at the anode as well as at the cathode side. In particular, this will be focused on the design of materials for the better performance and durability of MCFC.

## Acknowledgement

This work was financially supported by the Polish National Center for Research and Development in the framework of the Applied Research Program (Grant No. PBS3/B2/24/2015). We would like to thank G.J. Oliver for valuable comments on an earlier version of the manuscript.

## References

- [1] S. Torquato. *Random Heterogeneous Materials: Microstructure and Macroscopic Properties*. Springer, New York, 2013.
- [2] A. Wijayasinghe, B. Bergman, and C. Lagergren. LiFeO<sub>2</sub>–LiCoO<sub>2</sub>–NiO materials for molten carbonate fuel cell cathodes. Part I: Powder synthesis and material characterization. *Solid State Ionics*, 177(1):165–173, 2006.
- [3] D. Barsuk, A. Zadick, M. Chatenet, K. Georgarakis, N. T. Panagiotopoulos, Y. Champion, and A. Moreira Jorge. Nanoporous silver for electrocatalysis application in alkaline fuel cells, *Materials & Design*, 111(5): 528-536, 2016.
- [4] T. Kudo, Y. Hisamitsu, K. Kihara, M. Mohamedi, and I. Uchida. X-ray diffractometric study of in situ oxidation of Ni in Li/K and Li/Na carbonate eutectic. *Journal of Power Sources*, 104(2):272–280, 2002.
- [5] B. Huang, G. Chen, F. Li, Q. C. Yu, and K. A. Hu. Study of NiO cathode modified by rare earth oxide additive for MCFC by electrochemical impedance spectroscopy. *Electrochimica Acta*, 49(28):5055–5068, 2004.

- [6] S. G. Hong and J. R. Selman. A stochastic structure model for liquid-electrolyte fuel cell electrodes, with special application to MCFCs I. Electrode structure generation and characterization. *Journal of The Electrochemical Society*, 151(5):A739–A747, 2004.
- [7] S. G. Hong and J. R. Selman. Wetting characteristics of carbonate melts under MCFC operating conditions. *Journal of The Electrochemical Society*, 151(1): A77–A84, 2004.
- [8] P. Berg and J. Findlay. Mass transport phenomena in a MCFC cathode. *arXiv preprint arXiv:0909.0528*, 2009.
- [9] G. Özkan, S. Gemici, E. Başarir, and G. Özkan. Determination of optimum production conditions of casting slurry in the manufacture of molten carbonate fuel cell electrodes with the tape casting technique. *Chemical Engineering Transactions*, 52:871-876, 2016.
- [10] B. Huang, F. Li, Q. C. Yu, G. Chen, B. Y. Zhao, and K. A. Hu. Study of NiO cathode modified by ZnO additive for MCFC. *Journal of Power Sources*, 128(2):135–144, 2004.
- [11] T. Wejrzanowski, J. Skibinski, J. Szumbariski, and K. J. Kurzydłowski. Structure of foams modeled by Laguerre–Voronoi tessellations. *Computational Materials Science*, 67:216–221, 2013.
- [12] G. Gaiselmann, M. Neumann, L. Holzer, T. Hocker, M. Prestat, and V. Schmidt. Stochastic 3D modeling of  $\text{La}_{0.6}\text{Sr}_{0.4}\text{CoO}_{3-\delta}$  cathodes based on structural segmentation of FIB-SEM images. *Computational Materials Science*, 67:48–62, 2013.
- [13] M. Y. Ramandi, I. Dincer, and P. Berg. A transient analysis of three-dimensional heat and mass transfer in a molten carbonate fuel cell at start-up. *International Journal of Hydrogen Energy*, 39(15):8034–8047, 2014.
- [14] S. N. Chiu, D. Stoyan, W. S. Kendall, and J. Mecke. *Stochastic Geometry and its Applications*. J. Wiley & Sons, Chichester, 3rd edition, 2013.
- [15] C. Redenbach. Microstructure models for cellular materials. *Computational Materials Science*, 44(4):1397–1407, 2009.
- [16] T. Wejrzanowski, J. Skibinski, and K. J. Kurzydłowski. Modeling structures of cellular materials for application at various length-scales. *Computer Methods in Materials Science*, 13(4):493–500, 2013.
- [17] G. L. Lee, J. R. Selman, and L. Pomp. Comparison of MCFC cathode materials by porous electrode performance modeling. *Journal of The Electrochemical Society*, 140(2):390–396, 1993.
- [18] T. Wejrzanowski, M. Grybczuk, M. Chmielewski, K. Pietrzak, K. J. Kurzydłowski, and A. Strojny-Nedza. Thermal conductivity of metal-graphene composites. *Materials & Design*, 99:163–173, 2016.
- [19] K. Matouš, M. G. D. Geers, V. G. Kouznetsova, and A. Gillman. A review of predictive nonlinear theories for multiscale modeling of heterogeneous materials. *Journal of Computational Physics*, 330:192–220, 2017.
- [20] J. A. Prins-Jansen, K. Hemmes, and J. H. W. De Wit. An extensive treatment of the agglomerate model for porous electrodes in molten carbonate fuel cells–I. Qualitative analysis of the steady-state model. *Electrochimica Acta*, 42(23-24):3585–3600, 1997.
- [21] E. Fontes, C. Lagergren, and D. Simonsson. Mathematical modelling of the MCFC cathode. *Electrochimica Acta*, 38(18):2669–2682, 1993.

- [22] J. A. Prins-Jansen, J. D. Fehribach, K. Hemmes, and J. H. W. De Wit. A three-phase homogeneous model for porous electrodes in molten-carbonate fuel cells. *Journal of The Electrochemical Society*, 143(5):1617–1628, 1996.
- [23] W. Depczynski, R. Kazala, K. Ludwinek, and K. Jedynak. Modelling and microstructural characterization of sintered metallic porous materials. *Materials*, 9(7):567, 2016.
- [24] P. Bowen. Particle size distribution measurement from millimeters to nanometers and from rods to platelets. *Journal of Dispersion Science and Technology*, 23(5): 631–662, 2002.
- [25] T. Wejrzanowski, K. Cwieka, J. Milewski, and K. J. Kurzydowski. Optimization of the microstructure of molten carbonate fuel cell anodes. *Journal Science Forum*, 890:274–277, 2017.
- [26] N. Otsu. A threshold selection method from gray-level histograms. *IEEE Transactions on Systems, Man, and Cybernetics*, 9:62–66, 1975.
- [27] S. Plimpton. Fast parallel algorithms for short-range molecular dynamics. *Journal of Computational Physics*, 117(1):1–19, 1995.
- [28] LAMMPS. <http://lammps.sandia.gov/>, 2016.
- [29] J. M. Haile. *Molecular Dynamics Simulation*. J. Wiley & Sons, New York, 1992.
- [30] G. Taubin. Curve and surface smoothing without shrinkage. *IEEE Fifth International Conference on Computer Vision*, 852-857, 1995.
- [31] T. C. Lee, R. L. Kashyap, and C. N. Chu. Building skeleton models via 3-D medial surface axis thinning algorithms. *CVGIP: Graphical Models and Image Processing*, 56(6):462–478, 1994.
- [32] VSG - Visualization Sciences Group - Avizo Standard. <http://www.vsg3d.com/>, 2017.
- [33] T. Hildebrand and P. Ruesegger. A new method for the model independent assessment of thickness in three dimensional images. *Journal of Microscopy*, 185(1):67-75, 1997.
- [34] J. Ohser and K. Schloditz. *3D Images of Materials Structures: Processing and Analysis*. J. Wiley & Sons, Weinheim, 2009.
- [35] O. Stenzel, O. M. Pecho, L. Holzer, M. Neumann, and V. Schmidt. Predicting effective conductivities based on geometric microstructure characteristics. *American Institute of Chemical Engineers Journal*, 62:1834–1843, 2016.
- [36] J. Mayer, V. Schmidt, and F. Schweiggert. A unified simulation framework for spatial stochastic models. *Simulation Modelling Practice and Theory*, 12(5):307–326, 2004.

## Appendix A: LAMMPS simulation potentials

### Hertzian pairwise interaction (Gran/hertz/history)

This potential prevents spheres from collapsing, where the frictional force  $F_{hz}$  between two spheres with midpoints  $S_i$  and  $S_j$  and corresponding radii  $R_i$  and  $R_j$  is computed according to the following formula:

$$F_{hz} = \sqrt{\delta} \sqrt{\frac{R_i R_j}{R_i + R_j}} [(k_n \delta \mathbf{n}_{ij} - m_{\text{eff}} \gamma_n \mathbf{v}_n) - (k_t \Delta \mathbf{s}_t + m_{\text{eff}} \gamma_t \mathbf{v}_t)], \quad (1)$$

provided that their overlap distance  $\delta = R_i + R_j - d(S_i, S_j)$  is greater than zero, where  $d(S_i, S_j)$  denotes the distance between  $S_i$  and  $S_j$ . Here  $k_n$  and  $k_t$  are elastic constants for normal and tangential contacts,  $\gamma_n$  and  $\gamma_t$  are viscoelastic damping constants, and  $m_{\text{eff}}$  is the effective mass of the two particles. In our calculations, we assumed that  $k_n = 150000$  and  $k_t = 6000$ , which enabled efficient packing.

### Lennard- Jones potential (Lj/cut)

This is a common potential, which approximates the interaction between a pair of neutral atoms or molecules. However, in our studies we used the Lennard-Jones potential to model the particles behavior during the sintering process. The energy  $E$  controlling particles interaction is defined by the following formula:

$$E = 4\varepsilon \left[ \left( \frac{\sigma}{r} \right)^{12} - \left( \frac{\sigma}{r} \right)^6 \right], \quad r < r_c. \quad (2)$$

Here  $\varepsilon$  is a constant which is responsible for the strength of the bond,  $\sigma$  is the equilibrium length of the bond, and  $r$  is the distance between the centers of two spheres [26]. The cutoff distance  $r_c$  for each pair of nickel spheres is just set above the sum of their radii to affect and join only adjacent particles. A high value of  $\varepsilon = 10^6$  is assigned to create permanent bonds between sintered particles (spheres with a distance of less than  $r_c$  between each other). The equilibrium length  $\sigma$  is fitted by comparison of the simulated microstructures with the experimental ones, which leads to  $\sigma = 0.8 (R_i + R_j)$  where  $R_i$  and  $R_j$  are the radii of the considered interacting spheres.